

IMPACT OF INLET FLOW ON MACROSEGREGATION FORMATION ACCOUNTING FOR GRAIN MOTION AND MORPHOLOGY EVOLUTION IN DC CASTING OF ALUMINIUM

Akash Pakanati, Knut Omdal Tveito, Mohammed M'Hamdi, Hervé Combeau and Miha Založnik

Abstract

Several transport mechanisms contribute to macrosegregation formation in Direct Chill (DC) casting of aluminium. The latter include solidification shrinkage induced flow, thermal-solutal convection and grain motion. The relative importance of these transport mechanisms depends on process parameters such as cast velocity, inlet melt flow, cooling rate, cast dimensions etc. Of these, the inlet melt flow due to vertical jet is known to cause significant modification in macrosegregation by resuspending equiaxed grains at the center of the ingot/billet. In this paper, we investigate by means of modeling the macrosegregation formation due to an inlet vertical jet. For this purpose, a three-phase, multiscale solidification model accounting for above mentioned transport phenomena except for shrinkage induced flow is applied on a DC cast billet. The model considers grain motion accounting for both globular and dendritic equiaxed grain growth and we investigate their interaction with the inlet vertical jet. We show that an interplay of morphology evolution of equiaxed grains and inlet vertical jet together contribute to grain resuspension which in turn modifies macrosegregation formation. We also compare these results with a case with open inlet.

Keywords: Macrosegregation, Equiaxed Grains, DC-Casting, Resuspension

A. Pakanati

Dept. of Materials Technology, NTNU, N-7491 Trondheim, Norway

Email : akash.pakanati@ntnu.no

Telephone : +47 45243581

K. O. Tveito

Dept. of Materials Technology, NTNU, N-7491 Trondheim, Norway

Email : knutomda@gmail.com

Telephone : +47

M. M'Hamdi

SINTEF Materials and Chemistry, N-0314 Oslo, Norway

Email : Mohammed.Mhamdi@sintef.no

Telephone : +47 98283949

H. Combeau

Institut Jean Lamour, CNRS – Université de Lorraine, Campus Artem, 2 allée André Guinier, F-54000 Nancy, France

Email : herve.combeau@univ-lorraine.fr

Telephone : +33 372742683

M. Založnik

Institut Jean Lamour, CNRS – Université de Lorraine, Campus Artem, 2 allée André Guinier, F-54000 Nancy, France

Email : miha.zaloznik@univ-lorraine.fr

Telephone : +33 372742672

1. Introduction

Several transport mechanisms contribute to macrosegregation formation in DC casting of aluminium alloys [1]. Of these, sedimentation of equiaxed grains is considered as a significant cause for centreline solute depletion in DC cast products. Preventing sedimentation of equiaxed grains could potentially eliminate negative segregation at the center of the ingot/billet [2].

Zhang et al. [3, 4] conducted a series of DC cast billet experiments of AA7050 to study the impact of inlet melt flow on macrosegregation and microstructure formation. Of the two kinds of inlet melt flow, one involved a vertical jet. By using inlet jet, complete resuspension of the equiaxed grains away from the center of the billet was observed. In spite of this, Zhang et al. [3] observed severe solute depletion at the center of the billet due to washing away of the solute by the strong inlet vertical jet. Wagstaff and Allamore [2] conducted experiments on an ingot with Al - 4.5% Cu binary alloy. They directed vertical jet towards the center of the ingot and were successful in not only resuspending the grains, but also in eliminating negative segregation in the center of the ingot. Wagstaff and Allamore [2] proposed an optimal jet which had sufficient power to suspend grains and push them away from the center without causing excessive depletion. Nonetheless, there was no description of the grain morphology whereas Zhang et al. [3, 4] observed equiaxed dendritic grains.

The goal of this paper is to qualitatively discuss by means of modelling the impact of vertical jets with varying strength on macrosegregation formation of AA7050 alloy in a billet, accounting for equiaxed grain morphology. Based on this, we also discuss the link between grain morphology and inlet vertical jet leading to the resuspension of the equiaxed grains. For this, we employ a three-phase (solid, intragranular and extragranular liquid), multiscale solidification model accounting for thermal-solutal convection and grain motion (both globular and dendritic) based on the model described in Ref [5].

2. Numerical Model

The three phase, multiscale numerical model [5] is an extension of the two-phase solidification model proposed by Zaloznik and Combeau [6]. For a detailed description of the model the reader is referred to these articles. Only the main model features are described here.

The Euler-Euler volume-averaged model considers macroscopic transport and microscopic growth. The macroscopic transport accounts for solute and heat transport coupled to phase momentum transfer accounting for thermal-solutal convection and grain motion. For the sake of simplicity solidification shrinkage is not accounted for by considering equal and constant densities in solid and liquid phases. Boussinesq approximation is used for the liquid density in buoyancy term. For the solid phase, two flow regimes are considered depending on the envelope fraction (g_{env}).

For envelope fractions lower than a packing fraction (g_{pack}) the solid (equiaxed grains) is freely floating. The interfacial drag is modeled in the same manner as Ref. [6] for spherical particles but by considering the envelope fraction instead of solid fraction. The grain (solid) settling velocity $\vec{v}_s - \vec{v}_l$ is calculated using the algebraic relation described in Eq. (1). The description of the terms in the equation below are provided in Table 4.

$$\vec{v}_s - \vec{v}_l = \frac{4d_g^2(1 - g_{env})}{3g_{env}C_D\mu_l Re} [-g_s \nabla p_l + g_s \rho_{s,b} \vec{g}] \quad (1)$$

We can simplify the equation by applying the relation describing the internal solid fraction $g_{intern} = g_s/g_{env}$. This reduces to Eq. (2)

$$\vec{v}_s - \vec{v}_l = \frac{4d_g^2 g_{intern}(1 - g_{env})}{3C_D\mu_l Re} [-\nabla p_l + \rho_{s,b} \vec{g}] \quad (2)$$

where g_{intern} accounts for the grain morphology. A globular morphology corresponds to internal solid fraction values close to 1, whereas dendritic morphology is associated with low internal solid fraction values.

For envelope fractions greater than packing fractions, grains are assumed to form a rigid porous solid matrix moving with the casting velocity, \vec{V}_{cast} . The interfacial drag now is modeled by a Darcy term, where the permeability (K) is calculated from the Kozeny Carman relation for the character size, l_{KC} . This Darcy term is always limited to the upper bound of envelope fraction. The transition between free floating grains and rigid porous solid matrix is done explicitly by considering a hard numerical transition in the model. A Low Rayleigh number (LRN) turbulent energy-pseudoturbulent dissipation ($k - \epsilon$) model was used to address the turbulence problem.

The microscopic part is treated locally within each control volume and accounts for both nucleation and growth kinetics. Nucleation of grains is assumed to occur on grain-refiner (inoculant) particles. According to the athermal nucleation theory of Greer and co-workers [7], the critical undercooling for free growth of a grain on an inoculant particle of diameter d is given by $\Delta T_c = 4\Gamma_{GT}/d$ where Γ_{GT} is the Gibbs-Thompson coefficient. The number of activated particles then depends on the size distribution of the particle population, which can be represented by an exponential distribution density function. This representation holds for the largest particles, which are activated at small undercoolings and therefore successful as nuclei. This size distribution is then discretized into m classes of inoculants. Each class i is represented by a volumetric population density N_{nuc}^i and a critical undercooling ΔT_c^i . When the local undercooling reaches the critical undercooling of class i , its local inoculant density, N_{nuc}^i , is instantaneously added to the grain density, N_g , and N_{nuc}^i becomes locally zero. The model accounts for finite diffusion in both solid and liquid phases and local thermal equilibrium is assumed.

3. Problem Description

The test case we employ for conducting this study is based on the experiments conducted by Zhang et al. [3, 4]. The domain is modelled as a 2D axisymmetric problem as it can be seen in Fig. 1. Since we use a Euler-Euler framework based on well established theoretical work [6], the solid grains are also treated as a continuous phase similar to liquid phase. The assumption of symmetry applies to both the phases consequently. We consider a variable inlet radius of x mm taking the values of 10, 15 and 157.5 mm. By increasing the value of x from 10 to 15 mm we reduce the inlet jet intensity. Assigning $x = 157.5$ mm (radius of the billet) results in an open inlet. In this paper, a casting velocity V_{cast} of 90 mm/min is chosen and the inlet temperature (T_{cast}) of liquid metal is fixed at 680 °C. Detailed boundary are given in Table 1. The inlet velocity is calculated from the global mass balance. The primary and secondary cooling heat fluxes are modelled with a Fourier condition ($q = h(T_{amb} - T)$). The secondary cooling heat transfer coefficient is modelled by the correlation given by Weckmann and Niessen [8], as shown in Eq. (3)

$$h_{secondary}(T) = [-167000 + 352(T - T_{water})] * \left(\frac{Q_{water}}{P}\right)^{\frac{1}{3}} + 20.8 \frac{(T - T_{sat})^3}{(T - T_{water})} \quad (3)$$

Where T_{amb} is the ambient temperature, T is the surface temperature of the ingot, T_{water} is the water temperature, T_{sat} is the boiling temperature of the water, Q_{water} is the water flow rate, and P is the billet perimeter. All parameter values are given in Table 1.

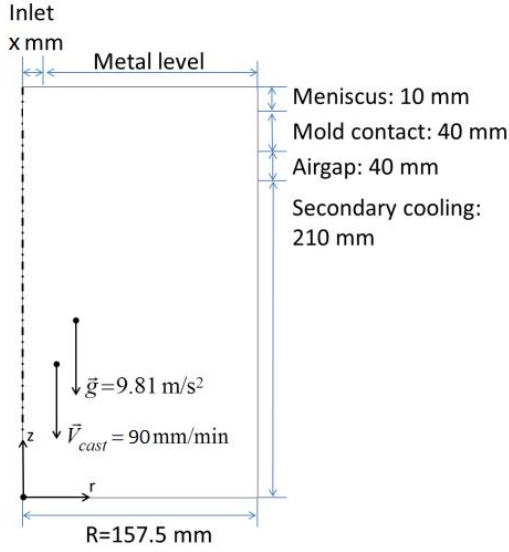


Fig. 1 Billet geometry with vertical inlet. Corresponding boundary conditions given in Table 1

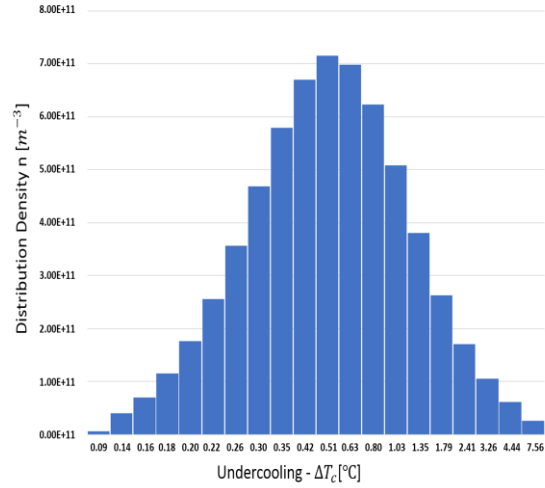


Fig. 2 Inoculant distribution

Table 1 Boundary Conditions for Energy, Liquid Momentum and Solid Momentum			
Boundary	Energy	Liquid Momentum	Solid Momentum
Inlet	$T_{cast} = 680 \text{ }^\circ\text{C}$	calculated	-
Metal Level	$h = 20 \text{ W}/(\text{m}^2\text{K}), T_{amb} = 100 \text{ }^\circ\text{C}$	Slip	-
Meniscus	$q = 0 \text{ W}/\text{m}^2$	No-slip	No-slip
Mold Contact	$h = 600 \text{ W}/(\text{m}^2\text{K}), T_{amb} = 20 \text{ }^\circ\text{C}$	No-slip	No-slip
Air Gap	$h = 120 \text{ W}/(\text{m}^2\text{K}), T_{amb} = 20 \text{ }^\circ\text{C}$	No-slip	No-slip
Direct Chill	Based on Equation (3) $T_{amb} = T_{water} = 20 \text{ }^\circ\text{C},$ $T_{sat} = 100 \text{ }^\circ\text{C},$ $Q_{water} = 40 \text{ l}/\text{min}$	No-slip	No-slip
Outlet	-	-	V_{cast}

The thermophysical data for the AA7050 alloy are given in Table 2 and the nomenclature can be found in Table 4. The linearized phase diagram defined by the liquidus slope, partition coefficient and the pure melting temperature, has been adjusted to fit the solidification path of AA7050 calculated from the microstructure code ALSTRUC [9]. The solute diffusion coefficients were calculated from [10] at the liquidus temperature of the nominal alloy. The packing fraction is set at 0.3. The density of solid accounting for buoyancy effects is assumed to be constant.

Table 2 Thermophysical data for AA7050 alloy used in the numerical simulations

Property	Unit	Value	Property	Unit	Value
c_p	J.kg ⁻¹ °C ⁻¹	1.3x10 ³	ρ_l	kg/m ³	2468.7
L_f	J kg ⁻¹	3.63x10 ⁵	ρ_s	kg/m ³	2468.7
Γ_{GT}	K.m	1.9x10 ⁻⁷	$\rho_{s,b}$	kg/m ³	2538.9
μ_l	N.S.m ⁻²	1.28x10 ⁻³	β_T	°C ⁻¹	-1.1 x10 ⁻⁴
κ_l	W.m ⁻¹ . °C ⁻¹	75.0	l_{KC}	m	7.5 x10 ⁻⁵
κ_s	W.m ⁻¹ . °C ⁻¹	185.0	g_{pack}	-	0.3
T_m	°C	667.0			
T_{eut}	°C	450.0			
Property	Unit		Zn	Mg	Cu
$C_{0,i}$	wt.%		6.24	2.05	2.12
$k_{p,i}$	-		0.39	0.29	0.09
$m_{l,i}$	°Cwt.% ⁻¹		-2.81	-3.88	-4.09
$D_{l,i}$	m ² s ⁻¹		2.682x10 ⁻⁹	7.326x10 ⁻⁹	4.372x10 ⁻⁹
$D_{s,i}$	m ² s ⁻¹		2.385x10 ⁻¹²	1.664x10 ⁻¹²	8.363x10 ⁻¹³
$\beta_{c,i}$	(wt.%) ⁻¹		-1.23 x10 ⁻²	4.0x10 ⁻³	-7.3x10 ⁻³

The size distribution for grain refiner particles is taken from [11] for 2 kg/ton of inoculants of type TiB₂. The distribution is modeled by an exponential function for inoculant diameters between 1 and 10 μm. The distribution density function of the population of inoculant particles, when, as usually, represented as a function of the particle diameter, is continuously decreasing. However, when expressed as a function of the critical undercooling, this distribution reaches a maximum at around 0.5 °C, as can be seen in Fig. 2. In the present study, the distribution is discretized into 20 classes with undercooling intervals defined by increasing step size from 0.1 to 2.1 °C as shown in Fig. 2.

The transport equations are solved with a Finite Volume Method and the SIMPLE-algorithm for staggered grid is used for pressure-velocity coupling. The convective terms are discretized with a first-order upwind scheme and for time discretization a fully implicit first-order scheme is used. For all simulations a structured grid of 8192 cells ($N_r \times N_z = 64 \times 128$) is employed. This results in an averaged edge length of 2.5 mm. Since the solid domain also behaves as a continuous phase, the current mesh resolution is sufficiently accurate to describe grain motion. The time step is set constant to 0.03 s and the simulations are run until steady-state condition.

4. Results and Discussion

An overview of all the cases system are summarized in Table 3. A total of six cases (1-6) based on the inlet radius value ($x = 10, 15$ and 157.5 mm) and grain growth model are considered. All the cases include the same transport mechanisms: forced convection ($x = 10$ & 15 mm), thermal-solutal convection and grain motion, in addition to forced convection for Cases 1, 2, . For Case 1, 2 and 3, the globular morphology is realized by imposing solid fraction as envelope fraction ($g_{env} = g_s$). Case 3 and 6 correspond to an open inlet condition for globular and dendritic grain growth model, respectively.

Table 3 Simulation Cases		
Case	Growth Model	Inlet radius (x)
1	Globular	$x = 10$ mm
2	Globular	$x = 15$ mm
3	Globular	$x = 157.5$ mm
4	Dendritic	$x = 10$ mm
5	Dendritic	$x = 15$ mm
6	Dendritic	$x = 157.5$ mm

Fig. 3a shows the macrosegregation pattern of Zn together with relative velocity $\vec{v}_l - V_{cast}$ vectors (black) for Case 1. The small inlet produces a vertical jet directed towards the center of the billet causing a counter clock wise flow loop. An other flow loop is observed away from the center which is clockwise in nature. Both loops collide around quarter distance from the center of the billet. The resulting solid fraction profile shows a "cliff" shaped (almost vertical solidification front) pattern around this region. At the center of the billet, macrosegregation formation is mainly due to washing of the solute due to the strong upstream flow due to forced convection. This can cause severe depletion near the cliff shaped region. In the mid-section, we also observe some depletion. The forced convection is not strong enough in this area and the major contribution for macrosegregation is globular grain settling indicated by $\vec{v}_s - \vec{v}_l$ vectors (white) in Fig. 3a. The grain settling is restricted mainly in the mid-section of the billet. In the center, the strength of the jet is strong enough to resuspend the grains and wash the solute away from the center of ingot. Fig. 4a shows the radial profile of relative segregation for Case 1 (blue). Due to combination of strong flow in the center and grain settling in the mid-section, severe solute depletion can be observed for most part of the billet. Close to the surface we notice positive segregation due to solute transport towards this region.

In Case 2, the inlet radius is increased to 15 mm. This results in a jet flow not strong enough to resuspend the globular grains. This can be seen in Fig. 3b where a larger region of grain settling is observed with the grains settling towards the center of the billet. Unlike Case 1, the inlet jet does not cause severe depletion of the solute at the center of the billet. The radial profile of macrosegregation for Case 2 (red) can be seen in Fig. 4a and negative segregation due to grain settling is observed towards the center of the ingot. Towards the surface, positive segregation is observed similarly to Case 1. In Case 3, we consider an open inlet by considering the inlet radius equal to the radius of the billet. This case can be similar to a case with an inlet melt flow and diffuser where there is limited vertical momentum. In the current case there is no forced convection and the driving forces are combination of globular grain transport and thermal-solutal convection. Zinc is heavier than Aluminium and this results in a co-operating thermal and solutal convection. Consequently, the thermal-solutal convection flow loop is clockwise in nature. The settling of the grains is towards the center of the billet resulting in a clockwise flow loop. Combination of these two effects results in reduced relative velocities between solid and liquid phase, a phenomena also observed and described in detail in Založnik et al. [12]. Even though we observe regions of grain settling in Fig. 3c marked with $\vec{v}_s - \vec{v}_l$ vectors (white), the grain settling intensity is reduced which in turn reduces the macrosegregation formation. The radial profile of relative macrosegregation for Case 3 (black) can be seen in Fig. 4a. A flat profile with almost no segregation is observed.

For Case 4, a dendritic grain growth model is employed. As the evolution of the envelope fraction differs from the solid fraction, the instant of grain packing occurs at a lower solid fractions for increasing degree of dendritic morphology. The radial profile of internal solid fraction ($g_{intern} = g_s/g_{env}$) at the packing is plotted in Fig. 4c for Case 4 (blue). The internal solid fraction profile at the center due to limited or non-existent grain motion is not plotted. From the mid-section towards the center, the internal solid fraction for Case 4 (blue) is of the order 0.4 indicating the presence of dendritic grains. Fig. 3d shows the macrosegregation pattern of Zn together with relative velocity $\vec{v}_l - V_{cast}$ vectors (black) for Case 4 over plotted with settling vectors (white). The flow pattern is very

similar to that observed in Case 1 where we consider globular grains. Vertical jet towards the center of the ingot results in resuspension of grains due to which grain settling occurs in the mid-section of the ingot. Since dendritic grains pack at lower solid fractions, the intensity of solute depletion is less severe when compared to Case 1 with globular grains. The relative radial segregation profile is plotted in Fig. 4b for Case 4 (blue).

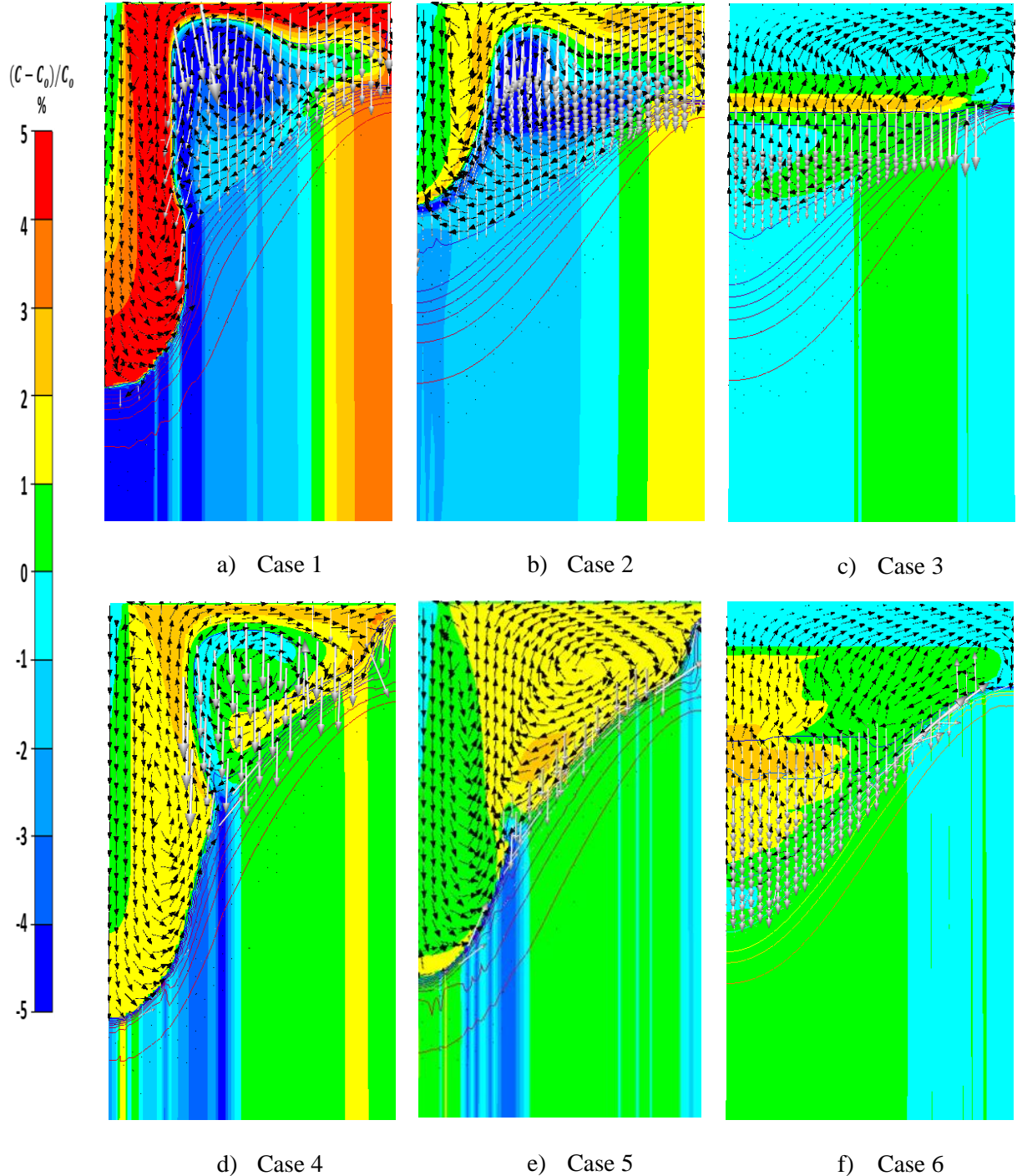


Fig. 3 Relative composition of Zn in % together with relative liquid velocity $\vec{v}_l - V_{cast}$ vectors (black), grain settling velocity $\vec{v}_s - \vec{v}_l$ vectors (white) and iso-lines of envelope fraction for Case 1 to 6 are shown. For Case 1, 2 and 3 the grains are assumed to be globular by imposing

$$g_{env} = g_s.$$

In Case 5, as the radius of the inlet is increased, the jet intensity is reduced. In spite of this, we observe resuspension of grains as can be seen in Fig. 3e. The latter contrasts with Case 2 (same inlet radius) for which the inlet jet did not result in resuspension of the grains. The main difference between Case 2 and 5 lies in the obtained grain morphologies. As shown in Eq. (2), relative velocities ($\vec{v}_s - \vec{v}_l$) are lower for dendritic grains ($g_{intern} < 1$) compared to the case of globular grains ($g_{intern} = 1$). In Case 5, the internal solid fraction is about 0.35 as can be seen from Fig. 4c. This results in reduced relative velocities and promotes resuspension of the grains for Case 5, as it can be seen in Fig. 3e. The relative radial segregation profile is plotted in Fig. 4b for Case 5 (red).

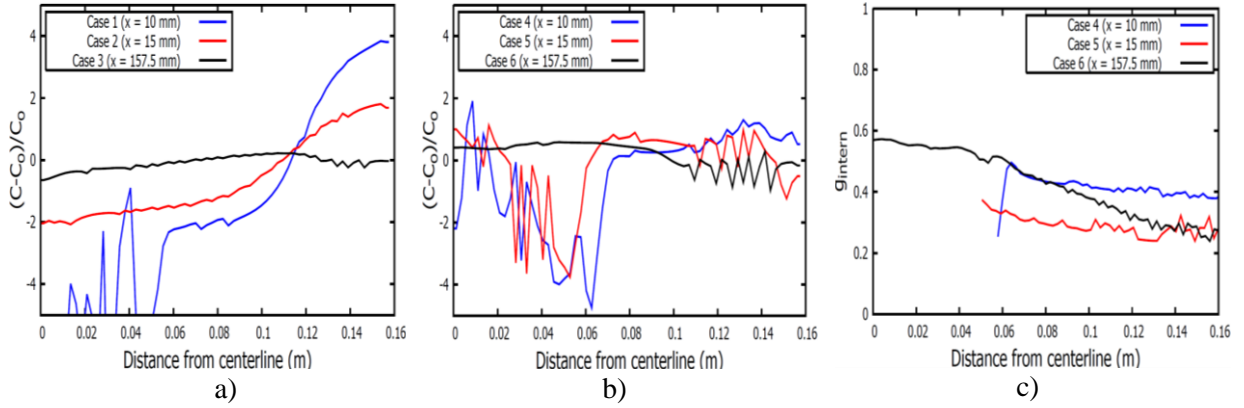


Fig. 4 a) Radial profile of relative macrosegregation for Cases 1, 2 and 3. b) Radial profile of relative macrosegregation for Cases 4, 5 and 6. c) Radial profile of internal solid fraction (g_{intern}) for Cases 4, 5 and 6.

In Case 6, we consider an open inlet and the only driving forces for macrosegregation are thermal-solutal convection and dendritic grain settling. Close to the surface, the grains are dendritic due to higher cooling rates and associated local undercooling as seen Fig. 4c. As we move towards the center of the billet, the cooling rate declines and grains become less dendritic. Close to the surface only a narrow region of grain motion is observed as the grains pack at a low solid fraction. Liquid flow through the packed region is possible as the permeability is sufficiently high. Consequently, the negative macrosegregation close to the surface as shown in Fig. 4b is primarily formed by thermal-solutal convection through the packed solid. Macrosegregation mechanism and the flow pattern towards the center of the billet in this case is similar to Case 3 with globular grains. This can be seen in Fig. 3e. However, the presence of dendritic grains in Case 6 results in slightly positive segregation towards the center of the billet as can be seen in Fig. 4b (black).

5. Conclusions

A three-phase, multiscale solidification model coupling macroscopic transport and equiaxed grain growth was used to study theoretically the impact of inlet jet intensity and grain morphology on macrosegregation. The intensity of inlet jet is controlled by changing the inlet radius. We have shown that inlet jet intensity can strongly affect macrosegregation formation in a DC cast billet by transport of equiaxed grains. We have also showed that the resuspension of grains is dependant not only on the inlet jet intensity but also on the morphology of the grain. Future work should focus on verifying these aspects experimentally.

Acknowledgement

This work is conducted within the framework of PRIMAL project with support from Hydro, Alcoa, Aleris, Research Council of Norway and NOTUR High Performance Computing program.

Table 4. Nomenclature

p_l	liquid pressure, Nm^{-2}	C_D	drag coefficient, -
g	volume fraction, -	d_g	diameter of the grain, m
t	time, s	\vec{g}	acceleration due to gravity, ms^{-2}
\vec{v}	intrinsic velocity, ms^{-1}		
K	permeability, m^2		Greek Symbols
T_{liq}	temperature of liquidus, $^{\circ}\text{C}$	ρ	density, kg/m^3
T_m	melting temperature of pure Al, $^{\circ}\text{C}$	μ_l	liquid dynamic viscosity, Pa s
T_{eut}	eutectic temperature, $^{\circ}\text{C}$	κ	thermal conductivity, $\text{W}\cdot\text{m}^{-1}\cdot^{\circ}\text{C}^{-1}$
Re	Reynolds number	β_T	thermal expansion coefficient, $^{\circ}\text{C}^{-1}$
c_p	specific heat, $\text{J}\cdot\text{kg}^{-1}\cdot^{\circ}\text{C}^{-1}$	$\beta_{C,i}$	solubility expansion coefficient of solute i, $\%w^{-1}$
L_f	Latent heat of fusion, $\text{J}\cdot\text{kg}^{-1}$		
l_{kc}	characteristic length for permeability, m		Subscripts and Superscripts
$D_{l,i}$	liquid diffusion coefficient of solute i, m^2s^{-1}	l	liquid
$D_{s,i}$	solid diffusion coefficient of solute i, m^2s^{-1}	s	solid
$m_{l,i}$	liquidus slope of solute i, $^{\circ}\text{C}\cdot\text{wt}\cdot\%^{-1}$	env	envelope
$k_{p,i}$	partition coefficient of solute i, -	s,b	solid buoyancy density
$C_{o,i}$	nominal concentration of solute i, %wt	$pack$	packing

6. References

- [1] R. Nadella, D. G. Eskin, Q. Du and L. Katgerman, "Macroseggregation in direct-chill casting of aluminium alloys," *Progress in Materials Science*, vol. 53, no. 3, pp. 421-480, 2008.
- [2] S. Wagstaff and A. Allamore, "Minimization of Macroseggregation in DC Cast Ingots Through Jet Processing," *Metallurgical and Materials Transactions B: Process Metallurgy and Materials Processing Science*, vol. 47, no. 5, pp. 3132-3138, 2016.
- [3] L. Zhang et al., "Effect of Inlet Geometry on Macroseggregation During the Direct Chill Casting of 7050 Alloy Billets: Experiments and Computer Modelling," *IOP Conference Series: Materials Science and Engineering*, vol. 33, pp. 1-8, 2012.
- [4] L. Zhang et al., "Influence of Melt Feeding Scheme and Casting Parameters During Direct-Chill Casting on Microstructure of an AA7050 Billet," *Metallurgical and Materials Transactions B*, vol. 43, no. 6, pp. 1565-1573, 2012.
- [5] M. Bedel, Étude de la formation des structures de solidification et des macroségrégations en coulée semi-continue d'aluminium, Nancy: PhD Thesis, 2014.
- [6] M. Založnik and H. Combeau, "An operator splitting scheme for coupling macroscopic transport and grain growth in a two-phase multiscale solidification model: Part I - Model and solution scheme," *Computational Materials Science*, vol. 48, no. 1, pp. 1-10, 2010.
- [7] A. L. Greer et al., "Modelling of inoculation of metallic melts: application to grain refinement of

- aluminium by Al-Ti-B," *Acta Materialia*, vol. 48, no. 11, pp. 2823-2835, 2000.
- [8] D. C. Weckman and P. Niessen, "A numerical simulation of D.C continuous casting process including nucleate boiling heat transfer," *Metallurgical and Materials Transactions B*, vol. 13, no. 4, pp. 593-602, 1982.
- [9] A. L. Dons et al., "The Alstruc microstructure solidification model for industrial aluminum alloys," *Metallurgical and Materials Transactions A*, vol. 30, no. 8, pp. 2135-2146, 1999.
- [10] Y. Du et al., "Diffusion Coefficients of some solutes in fcc and liquid Al: critical evaluation and correlation," *Materials Science and Engineering A*, vol. 363, no. 1-2, pp. 140-151, 2003.
- [11] A. Tronche, "Investigation of Modelling of Inoculation of Aluminium by TiC," *University of Cambridge*, 2000.
- [12] M. Založnik, A. Kumar, H. Combeau, M. Bedel, P. Jarry and E. Waz, "Influence of Transport Mechanisms on Macroseggregation Formation in Direct Chill Cast Industrial Scale Aluminum Alloy Ingots," *Advanced Engineering Materials*, vol. 13, no. 7, pp. 570-582, 2011.